Provided for non-commercial research and education use.
Not for reproduction, distribution or commercial use.

This article appeared in a journal published by Elsevier. The attached copy is furnished to the author for internal non-commercial research and education use, including for instruction at the authors institution and sharing with colleagues.

Other uses, including reproduction and distribution, or selling or licensing copies, or posting to personal, institutional or third party websites are prohibited.

In most cases authors are permitted to post their version of the article (e.g. in Word or Tex form) to their personal website or institutional repository. Authors requiring further information regarding Elsevier's archiving and manuscript policies are encouraged to visit:

http://www.elsevier.com/copyright

Author's personal copy

International Journal of Heat and Mass Transfer 54 (2011) 3394–3405

Contents lists available at ScienceDirect

International Journal of Heat and Mass Transfer

journal homepage: www.elsevier.com/locate/ijhmt

The temperature statistics of a surfactant-covered air/water interface during mixed convection heat transfer and evaporation

J. Kou, K.P. Judd, J.R. Saylor *

Department of Mechanical Engineering, Clemson University, Clemson, SC 29634-0921, United States

ARTICLE INFO

Article history:
Received 10 September 2010
Received in revised form 5 March 2011
Accepted 5 March 2011
Available online 16 April 2011

Keywords:
Evaporation
Free surface
Interfacial
Temperature statistics
Mixed convection
Surfactants
Turbulence
Air/water interface

ABSTRACT

Surface temperature fields were measured of an air/water interface where heat was transferred from the water to the air under mixed convection conditions. The interfacial temperature field was measured using an infrared (IR) camera for mean wind speeds ranging from 0 to 4.0 m/s, in 1.0 m/s increments. Statistics of these surface temperature fields, specifically, the root mean square (rms) and the skewness were obtained. Plots of the rms versus the heat flux showed linear behavior for low wind speeds (U = 0–3 m/s), and the skewness was also found to increase with heat flux for U = 0–3 m/s, although these data exhibited significant scatter. The scaled root mean square temperature was revealed to be governed by the ratio $Ra^{1/3}/(Re^{*4/5}Pr^{1/3})$ where Ra is the Rayleigh number, Re^* the Reynolds number based on water side friction velocity and Pr is the Prandtl number.

© 2011 Elsevier Ltd. All rights reserved.

1. Introduction

The transport of heat across an air/water interface is important in many aspects of limnology, oceanography and climatology and in several industrial applications. For the research reported here, the transfer of heat is considered from a warm body of water to a relatively cooler layer of air above. This research is motivated by thermal transport in small lakes and industrial cooling ponds, where depths are relatively small. Although much work has been dedicated to examining air–water interactions and surface structures in oceans, less research has been conducted on these smaller water bodies, in spite of their significance as freshwater resources [1]. We note that, because we consider the relatively shallow fluid layers typical of lakes and ponds, the entire fluid layer depth is used to characterize the buoyant instability. That is, the Rayleigh number which is used to characterize buoyancy induced flow (see below) is defined in terms of the total depth. This is significantly different from oceanographic studies, where the entire ocean depth does not participate in the natural convection process, and hence plays no role in understanding the buoyancy driven flows that may exist there.

The transfer of thermal energy from a warm body of water to the air above it can occur via natural or forced convection. Natural convection is caused by a buoyantly unstable flow configuration where the water near the free-surface cools, increasing its density until it sinks and is replaced by the warmer sub-surface fluid. At the same time, the layer of air immediately above the water surface is heated, rising upward and driving natural convection in the air as well. In forced convection, the transfer of heat is due to flow of the air and/or water by forces other than buoyancy. On the water side of the interface this transfer can be due to air flow above the interface which then results in flow of the liquid due to shear. Forced convection can also be due solely to flow on the liquid side due, for example, to the pumping of the liquid, although this mechanism is not considered in this paper.

Average wind speeds U over the surface of the ocean tend to be high, on the order of 7 m/s and much of the research on transport related to the air/ocean interface has focused primarily on forced convection [2]. However, for smaller water bodies such as lakes and ponds, wind speeds can be considerably smaller. For example, Klink [3] showed that for significant portions of the continental United States, the average wind speed is less than 3 m/s, particularly in the months of June, July and August. As another example, the average wind speed over Lake Sparkling in the US is 2.3 m/s [4], and the southeastern portion of the US experiences $U < 3$ m/s conditions for half of the year [3]. Similar results were reported by Deaves and Lines in the United Kingdom [5]. For this magnitude wind speed, both natural convection and forced convection contribute significantly to heat transfer (as shown in the next section), making heat transfer from lakes, ponds and other small water bodies a mixed convection problem.

* Corresponding author. Tel.: +1 864 656 5621; fax: +1 864 656 4435.
E-mail address: jsaylor@clemson.edu (J.R. Saylor).

0017-9310/$ - see front matter © 2011 Elsevier Ltd. All rights reserved.
doi:10.1016/j.ijheatmasstransfer.2011.03.047

Author's personal copy

Nomenclature

A	area
c_p	specific heat
g	gravitational acceleration
(i,j,k)	index of a pixel in three dimensional space of an IR image sequence
I	pixel intensity in an IR image
k	thermal conductivity
L	length
Pr	Prandtl number
q''	heat flux
Ra	Rayleigh number
Re	Reynolds number
Re^*	friction velocity based Reynolds number
Re_x	Reynolds number using x as the length scale
t	time
T	temperature
u_*	friction velocity
U	the wind speed
U_w	the water surface speed
x	downstream distance from the beginning of the wind tunnel
y	vertical distance from the wall
y^+	dimensionless vertical distance from wall

Greek symbols

α	thermal diffusivity
β	volume expansion coefficient
γ	skewness
ϵ	emissivity
ζ	surface tension
μ	dynamic viscosity
ν	kinematic viscosity
Π	surface pressure
ρ	density
σ	root mean square
τ	shear stress at wall

Subscripts

a	air
b	bulk water
s	surface
w	wall

The problem of interest here is to determine the relationship between the interfacial heat flux and the statistics of the surface temperature field for water bodies undergoing mixed convection. Such statistical relationships have been studied in the context of pure forced or pure natural convection, but much less so for mixed convection. Hence, attaining such a relationship is of some fundamental importance. An understanding of such a relationship may also enable the development of remote sensing methods for measuring the heat flux emanating from warm bodies of water such as cooling ponds in industrial sites and nuclear reactor cooling ponds, where the surface temperature field is measured by an aircraft or satellite-mounted IR camera. Such methods are needed, for example, in treaty verification applications and in ascertaining the efficacy of cooling ponds. Advances in remote sensing, namely the use of high spatial and temporal resolution infrared (IR) detectors, have begun to increase the possibilities that such methods can be developed. It should be noted, however, that such a method for remotely measuring heat flux would require understanding of other phenomena, including the effect of waves, solar reflection and reservoir inflows and outflows; hence the present work is just an initial step in this direction.

Studies of the relationship between the statistics of the surface temperature field and the interfacial heat flux are limited. Schimpf et al. [6] studied the air–water transport process by using a surface renewal model. The water surface temperature field statistics were computed, but their relationship with the interfacial heat flux was not studied. Garbe et al. [7] used passive thermographic and digital image processing techniques to measure the air/water interfacial temperature fields and to verify the surface renewal model of air–water heat exchange, showing the temporal variation of the temperature field and the heat flux, but without revealing the relationship between the surface temperature field statistics and the heat flux. Saylor et al. [8] studied the effect of surfactant monolayers on the pdfs and power spectra of the surface temperature field of a body of water undergoing free surface natural convection. These authors computed the rms and skewness of the surface temperature field, but only two values of the interfacial heat flux were investigated, preventing the development of a relationship between the heat flux and the statistics. In a subsequent study, Saylor et al. [9] investigated free surface natural convection in a warm tank of water in a quiescent air environment, computed the root mean square of the water surface temperature field and found a linear relationship between the rms and the interfacial heat flux. Mixed convection was not addressed in that study. Leighton et al. [10] conducted three-dimensional DNS simulations of heat transfer across an air/water interface where the liquid motion was due solely to buoyancy forces. They obtained the rms of the surface temperature field, as well as the profiles of the rms through the bulk fluid, and developed a scaling parameter to collapse these profiles. These studies are all relevant to the work presented here. However, for all but the work of Schimpf et al. [6] and Garbe et al. [7], the air side of the air/water interface was quiescent. Because actual lakes and cooling ponds are subjected to non-zero wind speed conditions, it is important to ascertain the effect of wind speed on the relationship between the rms of the surface temperature field and the heat flux.

Handler et al. [11] presented experimental results for an air/water interface under imposed winds from 1 to 4 m/s. IR images of the water surface were obtained, and the qualitative structure of the surface temperature field was compared to DNS simulations. However, statistical data were not presented in that work. The first study of the statistics of the surface temperature field of an air/water interface under finite wind speed was conducted by Conover and Saylor [12]. These authors explored the effect of wind speed on the relationship between the surface temperature field statistics and the interfacial heat flux for three wind speeds: 1, 1.8 and 2.6 m/s. Similar to Saylor et al. [9], Conover and Saylor [12] found a linear relationship between the rms of the surface temperature field and the heat flux for all three wind speeds investigated, showing that the addition of wind did not change the linearity of the relationship. Wind speeds greater than 2.6 m/s were not explored in the work of Conover and Saylor [12] due to problems associated with maintaining a homogeneous surfactant covered condition above 2.6 m/s, an issue that will be discussed further in this paper. To further the research in this area, one objective of the work presented here is to develop an experimental method capable of producing constant surfactant conditions at an air/water interface for a large range of wind speeds. Another objective is to explore the

Author's personal copy

behavior of the rms and skewness of the surface temperature field under conditions where both forced convection and natural convection are important to the interfacial heat transfer process.

Finally, we note that there is a body of literature on channel flows which is somewhat similar to the problem considered here. In channel flows there is a free surface, however the liquid flow is driven by some external pressure gradient, while here the liquid is driven either by buoyancy alone or by buoyancy in concert with flow due to wind shear at the interface. This difference is significant because in the case of the channel flow, significant turbulence is generated by the liquid flow over the channel floor, while in the present study turbulence from shear on the floor is small compared to the wind sheared air/water interface. The difference between these two cases notwithstanding, the qualitative nature of the surface temperature fields are remarkably similar for these two types of flow. Examples of such studies include those of Handler et al. [13], who conducted DNS simulations of a channel flow with a shear-free interface and obtained rms versus depth profiles for a constant heat flux at the interface. Handler et al. [14] conducted a similar DNS simulation for the case where the air/water interface was covered with a surfactant monolayer. Both of these simulations considered temperature as a passive scalar; no buoyancy forces existed. Enstad et al. [15] conducted DNS simulations of a channel flow for a stably stratified condition, an interesting counterpoint to the current work. However, that work did not include the rms of the surface temperature field.

2. Experimental method

2.1. Experimental facility

The experiments reported here were performed in the facility illustrated in Fig. 1(a), consisting of an insulated water tank beneath an open loop wind tunnel, an infrared (IR) camera and two thermocouples. The walls of the wind tunnel were fabricated from clear polycarbonate. Because polycarbonate is opaque to the IR wavelengths collected by the camera used here, a 16.51 × 16.51 cm opening in the roof of the wind tunnel was created to provide optical access. The main facility dimensions are given in Fig. 1(b). The tunnel plenum was designed to refine the incoming air flow to provide a uniform velocity entering the tunnel. In the direction of the air flow, the plenum was composed of a 3.18 cm thick layer of filter fabric, a 1.27 cm thick layer of Garolite honeycomb, a 5.72 cm spacer, a fine screen, a second 1.27 cm thick Garolite honeycomb layer, a second 5.72 cm spacer, a 1.27 cm thick layer of aluminum honeycomb, a third 5.72 cm thick spacer, and finally a coarse screen. The cross-section of the tunnel plenum was the same size as that of the wind tunnel. A rubber diffuser attached the blower to the tunnel plenum, eliminating the transmission of vibrations from the motor to the tunnel. A direct drive, three-phase motor/controller unit provided power to the blower.

The water tank had a volume of 27.04 L and was constructed from 0.635 cm thick plate glass. The bottom and sides of the tank were covered with insulating material to reduce heat loss. The tank fitted snugly in the wind tunnel test section. A thermocouple for recording the bulk water temperature T_b was threaded down the inside corner of the downstream location of the tank and positioned at the geometric center of the tank.

The thermal imaging system used to determine the surface temperature field was an Inframetrics Thermacam model SC1000 focal plane array camera with a 255 × 239 pixel sensor and a thermal resolution of 0.07 K. The camera was sensitive to infrared light in the 3.4–5 μm wavelength band. The mean optical depth of water at these wavelengths is 35 μm [16]. Thus, after proper calibration, IR images obtained in this wavelength band are surface

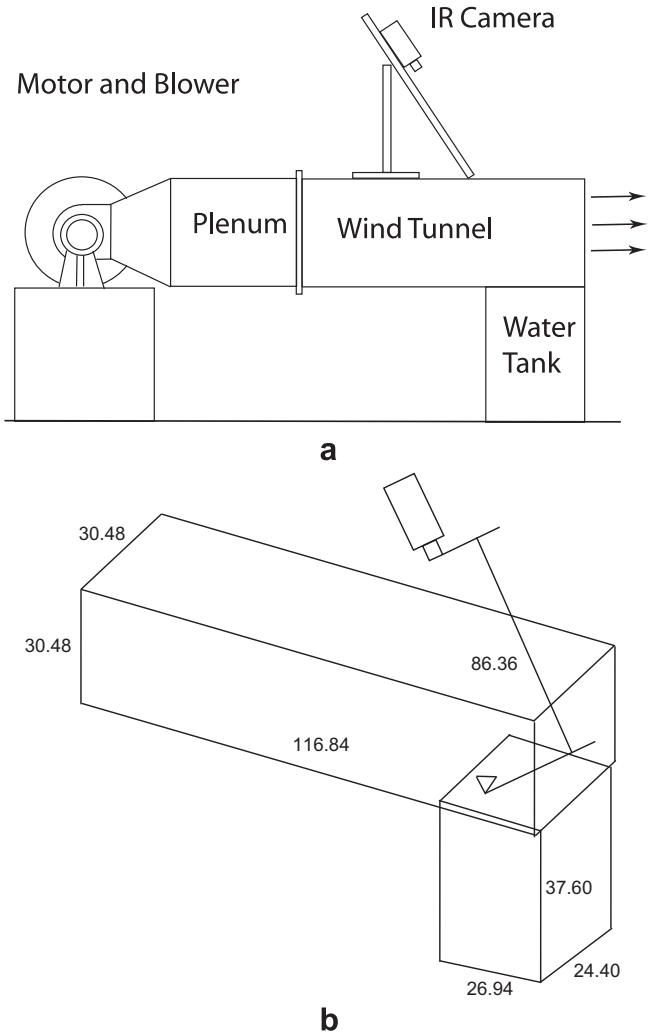

Fig. 1. Experimental facility: (a) schematic of the setup , (b) facility dimensions in centimeters.

temperature fields. The camera provided 12-bit TIFF images as output. The incline of the camera mount was 16° from vertical, which prevented the camera from imaging its own reflection on the water surface.

Any air/water transport experiment must address the presence of surfactant monolayers at the interface which can have important effects on all aspects of air/water transport [17–23]. Especially relevant to this work was the effect that such monolayers have on the hydrodynamic boundary condition at the air/water interface. Surfactants impart elasticity to an air/water interface, damping turbulence in the region near the interface, significantly affecting transport across that interface. As a result, experiments should be conducted either for interfaces that are clean and devoid of such monolayers or interfaces with a uniform monolayer having a repeatable surface concentration for all experiments. Here, surfactant covered conditions were explored since such conditions are virtually always the case for the lakes and ponds that motivate this research. The surfactant used was oleyl alcohol, which is well-characterized and often used as a proxy for surfactants found in natural bodies of water [24]. Because deionized water was not needed in this situation, tap water was used.

Although indigenous organic compounds exist in tap water and result in the formation of a monolayer that completely covers the water surface, preliminary experiments revealed that such monolayers failed to maintain coverage above wind speeds of ~3 m/s

Author's personal copy

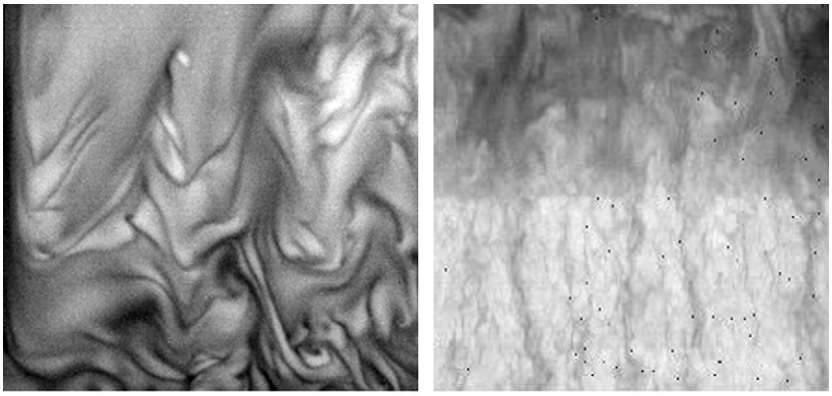

Fig. 2. IR images: (a) for a water surface having a coherent surfactant film at $U = 1.8$ m/s, and (b) for a surface with a Reynolds ridge at $U = 4$ m/s. In (b) the upstream region is clean and the downstream region is surfactant covered. The air flow is from bottom to top in both images. In these IR images, cold regions are dark and relatively warm regions are bright.

in this facility. As shown by Saylor [25], the presence of a monolayer is easily identified in IR imagery of a water surface undergoing natural convection as a cooler (darker) region containing fewer small scale structures than a clean surface. Two IR images taken during preliminary experiments are presented in Fig. 2. Fig. 2(a) shows an IR image of the water surface at the relatively low wind speed of 1.8 m/s. The structures present are typical of a surface sheared by wind and completely covered with a surfactant monolayer. Fig. 2(b) is an IR image for a wind speed of $U = 4$ m/s showing a relatively sharp demarcation between an upstream region (lower portion of the image), where the monolayer has been pushed downstream, and the downstream region where a compressed monolayer exists. The line separating the clean region and the monolayer covered region is referred to as a Reynolds ridge [26]. It is noted that bad pixels can be seen in these and subsequent IR images. These are pixels whose response is essentially constant regardless of the scene and, hence, were easily identified and were not used in any computations. Only 67 bad pixels exist in the (255×239) pixel array, insignificantly affecting the total data volume.

The formation of a Reynolds ridge presents a problem in this research since it prevents a meaningful comparison between the low wind speed results where the surface is covered with a homogeneous film and the high wind speed results where such a homogeneous surface condition is absent. In the research reported here, two procedures were implemented to prevent the formation of such a Reynolds ridge and to maintain a coherent monolayer up to a wind speed of 4 m/s. First, instead of locating the water tank at the immediate exit of the plenum, an artificial beach in the form of a flat acrylic plate, 88.9 cm long, was positioned immediately upstream of the water tank as shown in Fig. 1(a). Because the wall shear stress decreases with downstream position, inclusion of this beach reduces the net shear experienced by the monolayer for a given wind speed. For example, for a laminar boundary layer over a solid wall with no streamwise pressure gradient, the wall shear stress is [27]:

$$\tau_w = \frac{0.332\rho U^2}{\sqrt{Re_x}}, \tag{1}$$

where

$$Re_x = \frac{Ux}{\nu}, \tag{2}$$

ρ is the air density, x the downstream position, and ν the kinematic viscosity. Because the shear varies as $x^{-1/2}$, the upstream plate reduces the shear imposed by the wind on the monolayer, for a constant wind speed.

The second procedure used to maintain a coherent film was to remove the indigenous surfactant film that formed on the water surface and replace it with an excess of surfactant of a known composition, oleyl alcohol in this case. An excess of this surfactant was placed in a surfactant reservoir located at the downstream corner of the water tank as shown in Fig. 3(a) and (b). This surfactant reservoir consists of a piece of Teflon tubing 2.54 cm long with an inner diameter of 0.635 cm and a narrow slit running the length of the tube. The tube was held in place using a silicone sealant so that the top of the tube resided approximately 1 mm above the tank rim. An equilibrium spreading pressure (ESP) monolayer is one which forms when the monolayer spreads outward from an excess of surfactant. This spreading occurs when a monolayer forms from a liquid lens on the water surface for a liquid surfactant such as oleyl alcohol [28,29]. By placing an excess of oleyl alcohol in the reservoir, an ESP monolayer was created, and any loss of surfactant (due to, for example, evaporation of the surfactant or perhaps deposition at the water/glass contact line) was immediately

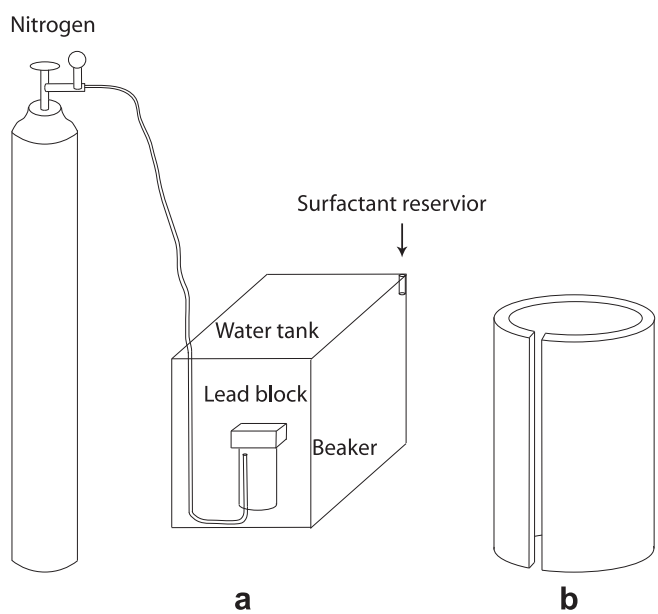

Fig. 3. The surfactant reservoir and the water leveling system: (a) the water leveling system with the surfactant reservoir, (b) the surfactant reservoir.

Author's personal copy

replaced by surfactant spreading from the reservoir through the slit. This second procedure was especially important since preliminary experiments showed that simply creating an oleyl alcohol monolayer would result in a coherent film for a period of time but that a Reynolds ridge would form later in the experiment, showing that surfactant was lost over time. By periodically adding surfactant to this reservoir, a monolayer was maintained for an unlimited period of time for wind speeds up to and including 4.0 m/s.

The equilibrium spreading pressure of oleyl alcohol at 25 °C is Π^e = 30.5 dyne/cm [30] where the spreading pressure, Π is defined as:

$$\Pi = \zeta_0 - \zeta, \tag{3}$$

and ζ_0 is the surface tension of a clean surface. Using a value of 72 dyne/cm for the surface tension of clean water gives a value of ζ = 41.5 dyne/cm, which is taken as the surface tension of the experiments presented herein.

Preliminary experiments also showed that a decrease in the water level due to evaporation caused the formation of resonant waves on the surface during the course of an experiment. To address this issue and to maintain a water surface flush with the upstream beach, a water leveling system was implemented which consisted of a 500 ml beaker positioned upside down on the bottom of the tank with pliable hypodermic tubing fixed to the inside, as shown in Fig. 3(a). Nitrogen gas was periodically fed from a gas cylinder through a pressure regulator to a precision ball valve and then to this hypodermic tubing. Whenever there was a noticeable drop in the water level (typically ~5 mm), the ball valve was carefully actuated, slowly releasing nitrogen into the beaker and displacing enough water to return the free surface to its original level. This was typically done every 20 min. To minimize the effect of the tubing on the fluid flow, it was threaded down the back corner of the water tank, in a fashion similar to that for the thermocouple wire. A lead block 37 × 43 × 89 mm was placed on top of the beaker to keep it in place. This block was coated with silicone sealant (GE RTV 118) so that the tank water was not exposed to lead. For all experimental runs, a graduated millimeter scale was taped to the inside of the tank to monitor water level changes.

The bulk water temperature T_b was recorded using a digital data logger (Digi-Sense model 91100–50) and a thermocouple probe (*E*-type) located at the geometric center of the tank. The air temperature T_a was recorded with the same data logger using another thermocouple located in the plenum housing. Both temperature probes had an uncertainty of ±0.1 °C. The wind speed, measured with a hand-held anemometer (Kestrel 1000), was found to vary by ±0.1 m/s. The nominal wind speed in the tunnel was taken to be the average of the measurements at two streamwise locations: the leading edge of the tank and the outlet of the tunnel. At both locations, the meter was placed on a slender rod with the metering section located at the geometric center of the tunnel cross section. Velocities ranging from 0 to 4 m/s in 1 m/s increments were explored.

2.2. Calibration

The IR camera was calibrated to a black body radiation source (Infrared Systems Development Corporation model IR-140/301 Black Body Source and Controller). During calibration, the lens of the camera was positioned 86.36 cm from the surface of the black body, the same distance the lens was positioned from the water surface during the experiments. Once the black body achieved a steady-state condition at the desired temperature, sixteen 12-bit TIFF calibration images were taken. This procedure was repeated for temperatures ranging from 27.5 to 50 °C in increments of 2.5 °C, for a total of 10 temperatures. The black body was 30.48 × 30.48 cm in size with a variation of ±0.5 °C across that area. To reduce the effect of this variation on the calibration, only the 60 × 50 pixel central region of the images was used to obtain the calibration equation relating the temperature T to the pixel intensity I.

A fourth order polynomial was obtained by fitting the temperature of the black body to the average intensity of the camera signal. This equation was:

$$T(I) = -4.8481 \times 10^{-16} I^4 + 4.3748 \times 10^{-11} I^3 - 1.5318 \times 10^{-6} I^2 + 0.0268 I - 140.1917, \tag{4}$$

where I is in counts (16-bit integers) and T in °C. If the intensity of a radiating black body is known, its temperature can be determined using Eq. (4). Due to the nonunity emissivity of a water surface, this equation cannot be applied directly here due to reflection of the surrounding radiation by the water surface. To account for this radiation, the water surface was assumed to be gray and diffuse. Under these assumptions, the relationship between the intensity measured by a pixel observing the water surface I_{out} and the intensity that would be observed had the water been a perfect black body $I(T_s)$ is:

$$I_{out} = \epsilon I(T_s) + (1 - \epsilon) I(T_{bg}), \tag{5}$$

where T_s is the water surface temperature, and T_{bg} is the background temperature which was assumed to be 23 °C (the measured air temperature) and to emit as a black body. The water surface temperature was obtained by first obtaining $I(T_s)$ from Eq. (5) and then solving for T_s by inverting Eq. (4). The emissivity of a water surface at the IR wavelengths sensed by the camera used here was ϵ = 0.9802 [12].

2.3. Experimental procedure

Prior to each experimental run, the water tank was cleaned thoroughly with methanol (spectrophotometric grade) and laboratory wipes (Kimberly-Clark), in part to remove any residual artificial contamination resulting from the previous run. The tank was filled to the rim with hot tap water, which was typically at 42 °C. If higher temperatures were needed, resistance-element heaters were used. The water surface was cleaned prior to application of the surfactant to ensure a consistent initial condition from run-to-run. The initial cleaning of the water surface was achieved using a clean wipe which was spread over the interface and pulled back, dragging the surface layer off. The surface temperature field was constantly monitored with the IR camera during this process. When the images were largely populated by small scale thermal structures for more than one minute, it was deemed clean (see [12]), and oleyl alcohol was applied to the water surface. A solution of 1 g of oleyl alcohol in 100 ml of heptane was prepared for the application of surfactant. To achieve an ESP monolayer, a 40 μl quantity of this solution was initially applied to the water surface, and the subsequent evaporation of the heptane left a monolayer of oleyl alcohol. The surfactant solution was applied with a microsyringe to the surfactant reservoir (shown in Fig. 3(b)). During the process of an experimental run, 20 μl of the oleyl alcohol solution was added about every 20 min to make up the loss of the surfactant due to evaporation.

Air and water temperatures were recorded every 20 s and IR images were recorded every 10 s. Sets of 96 images were acquired, which are referred to here as image sequences. These image sequences were subsequently processed to obtain a single statistical data point (rms and skewness). A range of heat fluxes was attained by running these experiments in a cool-down mode. As the tank cooled, the temperature difference between the air and the water decreased, resulting in a continuously decreasing heat

Author's personal copy

flux throughout the course of an experimental run. The system was assumed to be in a quasi-steady-state condition during each image sequence, and a single heat flux and set of statistics was computed for each sequence as shown below. Several sequences were acquired over the several hours duration of a run, the exact number of sequences depending on the wind speed and cool-down rate. The quasi-steady-state assumption was validated *a posteriori* by computing the changes in heat flux from the beginning to the end of each image sequence. The maximum heat flux change from all sequences for each wind speed is listed in Table 1 and ranges from 3.44% to 5.39%, sufficiently small to justify the quasi-steady-state assumption.

2.4. Data reduction

The heat flux at the water surface q'' was obtained by first computing the total tank heat loss and then correcting for losses through the insulated tank walls. The total tank heat loss is:

$$q_{\text{out}} = \frac{dT_b}{dt}\rho V c_p, \tag{6}$$

where ρ is the water density, V the tank volume, and c_p the specific heat of water. The loss of heat through the tank walls was determined through a separate set of "closed-top" experiments where the top of the tank was fitted with insulation, and the rate of decay of the bulk water temperature was due solely to heat leakage through the insulation. This wall heat loss is:

$$q_{\text{loss}} = \frac{dT_{b,c}}{dt}\rho V c_p, \tag{7}$$

where $\frac{dT_{b,c}}{dt}$ is the time rate of change of the bulk water during these closed-top experiments. The value of the heat flux, corrected for the wall loss is:

$$q'' = \frac{q_{\text{out}} - (q_{\text{loss}})\left(f_{\frac{5}{6}}\right)}{A_s}, \tag{8}$$

where A_s is the water surface area and $f_{\frac{5}{6}}$ is the ratio of the insulated areas for the open-top experiment (the regular experiment), to the insulated areas for the closed-top experiment, and accounts for the fact that the loss of heat through the tank walls for a regular experiment occurs through five walls, while during the closed-top experiments, it occurs through six walls. The corrected heat flux described by Eq. (8) is what is presented in the Results section of this paper.

Eqs. (6) and (7) require the time rate of change of T_b. This rate was obtained by first fitting the $T_b(t)$ data using an exponential. Values for dT_b/dt were then obtained by taking the derivative of this fit. Each image sequence lasted 16 min.

The definitions of the rms and skewness are:

$$\sigma = \sqrt{\frac{\sum_i \sum_j \sum_k \left(T_{i,j,k} - T_m\right)^2}{N-1}}, \tag{9}$$

and

$$\gamma = \frac{1}{N}\sum_i \sum_j \sum_k \left(\frac{T_{i,j,k} - T_m}{\sigma}\right)^3, \tag{10}$$

respectively, where $T_{i,j,k}$ is the temperature at pixel (i,j,k) obtained from an IR image, T_m is the appropriate average temperature, and N is the total number of pixels used in computing either σ or γ. As will be shown in the next section, the average temperature fields exhibited some spatial variations, and hence the method by which σ and γ were computed had to be chosen carefully. The (i,j,k) notation refers to the temperatures of a given pixel in the three dimensional space created by an image sequence, where i and j indicate a pixel's row and column positions in an IR image and k gives the index of the image which this pixel belongs to.

2.5. Uncertainty analysis

The following uncertainties were considered in the temperatures measured at each (i,j,k) location: (i) the spatial variation in the black body, (ii) the spatial variation in the sensitivity of the IR camera sensor, (iii) the temporal variation in the black body temperature, and (iv) the resolution of the IR camera. The resulting 95% confidence interval uncertainty in the surface temperature measurement ranged from ±0.0913 to ±0.117 °C, for the range of temperatures investigated. Uncertainty in heat flux measurement are due to the resolution of the thermocouple, the measurement of the water tank dimensions and the variation in heat flux during a sequence. The resulting 95% confidence interval uncertainty in heat flux was 9.31–49.5 W/m^2, over the range of heat fluxes measured.

2.6. Flow conditions

The air-side Reynolds number Re and the air-side Rayleigh number Ra for each of the non-zero wind speed cases investigated are presented in Table 2. The numbers were computed using the physical properties of air at 25 °C. The Reynolds number presented in Table 2 is defined:

$$Re = \frac{UL}{\nu}, \tag{11}$$

where U is the wind speed, L is the length from the leading edge of the artificial beach to the middle of the tank, and ν the kinematic viscosity of the fluid. The Rayleigh number is defined as:

$$Ra = \frac{g\beta L^4 q''}{\alpha \nu k}, \tag{12}$$

where g is the gravitational acceleration, β the volume expansion coefficient at constant pressure, L the tank depth, α the thermal diffusivity, and k the thermal conductivity. Although Re on the air-side is less than the typically accepted critical value $Re_c = 5 \times 10^5$ for transition to turbulence, [31] turbulent natural convection is generally accepted to begin at $Ra = 10^5$–10^8, and so the flow on the air side is presumed turbulent [32,33].

Table 3 presents the relevant dimensionless groups for the water side of the interface. Since the water velocity was not directly measured, some ambiguity exists over what velocity to use in computing the Reynolds number. Work conducted in a

Table 1
Maximum heat flux change for image sequences under wind speeds from 0 to 4 m/s.

Wind speed (m/s)	Maximum $\Delta q''$ (W/m^2)	Maximum $\Delta q''$ (%)
0	28.3	4.15
1	25.9	3.44
2	37.8	3.66
3	54.8	4.14
4	97.8	5.39

Table 2
The Reynolds numbers and the Rayleigh numbers for the air flow.

U (m/s)	Re	Ra
1	67,200	1.35–2.63×10^{10}
2	134,000	1.99–3.58×10^{10}
3	202,000	2.35–4.55×10^{10}
4	269,000	3.09–6.49×10^{10}

Author's personal copy

Table 3
Re, *Ra*, and the parameter defined in Eq. (13) for the water side of the interface.

U (m/s)	U_w (m/s)	u^*(cm/s)	Re	Ra	$\frac{Ra^{1/4}}{Re^{1/2}Pr^{1/3}}$
1	0.01	0.04	3860	$3.74–9.56 \times 10^{11}$	1.84–2.01
2	0.02	0.07	7660	$0.537–1.36 \times 10^{12}$	1.43–1.59
3	0.03	0.09	11380	$0.611–1.76 \times 10^{12}$	1.21–1.37
4	0.04	0.17	15140	$0.780–2.53 \times 10^{12}$	0.891–1.25

circular wind/water tunnel due to Jähne et al. [34] suggests that the water speed ranges from 3% to 4% of the wind speed. Here we measured the surface speed of the water by imaging the displacement of small Styrofoam particles placed on the water surface and found the surface speed to be 1% of the wind speed, a number which we used here to compute *Re* and is tabulated as U_w in Table 3. The Reynolds and Rayleigh numbers presented in Table 3 were computed using properties at the average water temperature for the experiments for each wind speed. The large values for *Ra* indicate that the water side flow is turbulent.

A criterion for the transition between natural convection dominated flow and forced convection dominated flow for a fluid is presented by Bejan [35] for $Pr > 1$ as:

$$\frac{Ra^{1/4}}{Re^{1/2}Pr^{1/3}} \begin{cases} > O(1), \text{Natural convection} \\ < O(1), \text{Forced convection} \end{cases}, \tag{13}$$

where the Prandtl number is defined as:

$$Pr = \frac{\nu}{\alpha}. \tag{14}$$

This ratio is also presented in Table 3 for each wind speed, and is of order unity for all wind speeds considered here, showing that the water flow is always in the mixed convection regime for this work.

In later sections of this paper, the friction velocity on the water side of the interface, u^* is used to define the Reynolds number (Re^*) when correlating our results (*viz.* not U_w), where u^* is defined as:

$$u^* = \sqrt{\tau_s/\rho}, \tag{15}$$

where ρ is the water density and τ_s is the shear stress at the air/water interface:

$$\tau_s = \mu \frac{du}{dy}, \tag{16}$$

where du/dy is the air side velocity gradient at the interface, and μ is the dynamic viscosity of air. This is to conform to the literature, where u^* tends to be used to parameterize air/water phenomena [36,37].

Obtaining u^* requires the velocity profile over the water surface so that du/dy can be computed. This velocity profile was obtained using a hot-film anemometry system consisting of a TSI IFA-100 anemometer and a TSI 1210 hot film sensor (200 μm diameter). The hot-film probe was calibrated with a TSI 1127 calibrator and a TSI IFA-300 constant temperature analyzer. The sensor was mounted on a Velmex high resolution vertical traverse. Velocities were recorded from the plate surface to the mid-plane of the wind tunnel. The overall setup is presented in Fig. 4. Velocity profiles were measured at two positions: 1 cm upstream of the tank edge above the solid plate and in the middle of the tank above the water surface. It is well known that thermal anemometry is inaccurate near a solid wall due to heat loss to the wall [38]. These errors were accounted for using the linear profile in the region between $y^+ = 5$ and $y^+ = 11$ to compute the gradient, since this region is unaffected by wall heat loss [38–40]. There is no research available which demonstrates a method for correcting the velocity profile for heat loss from the probe above a free surface, and so here we use the velocity gradient obtained at the upstream location above the solid plate to obtain u^*.

Using Re^* instead of *Re* to compute the ratio presented in Eq. (13) increases this ratio by a factor of ~ 5. However, within an order of magnitude, this still signifies the existence of mixed convection on the water side.

3. Results

3.1. Sample temperature fields

Sample temperature fields obtained at the five wind speeds considered here are presented in Fig. 5(a)–(e). These and all subsequent images are 22 cm in the cross-stream direction and 20 cm in the streamwise direction. For presentation purposes, the contrast of these fields was adjusted for this figure so that the range in temperatures filled the grayscale, allowing easier comparison of the structures in each image. Although the heat flux varies from image to image in Fig. 5(a)–(e), each was taken at the high end of the heat flux range for that wind speed. As Fig. 5(a)–(e) shows, the structures of the temperature fields qualitatively change as the wind speed increases. Specifically, in Fig. 5(a) and (b), the structures are relatively isotropic, showing no obvious evidence of the wind direction. In Fig. 5(c), the structures exhibit some evidence of the wind direction. In Fig. 5(d) the structures have become stretched in the streamwise direction, resulting in a narrowing in the cross-stream direction. At 4 m/s (Fig. 5(e)) the structures are different from those seen in the lower wind speed images. This difference may be due to recirculation in the water tank as is further discussed in Section 4, which causes these 4 m/s results to exist as outliers, compared to the other cases. Accordingly, this wind speed is excluded when presenting some of the subsequent statistical results.

Temperature fields for four different values of heat flux q'' obtained at a fixed wind speed of 3 m/s are presented in Fig. 5(f)–(i). The heat flux increases from left to right. The structures are all qualitatively similar in shape, with the primary visual effect of increasing heat flux being a decrease in the size of the structures. Since the wind speed is constant, the only parameter that is changing is

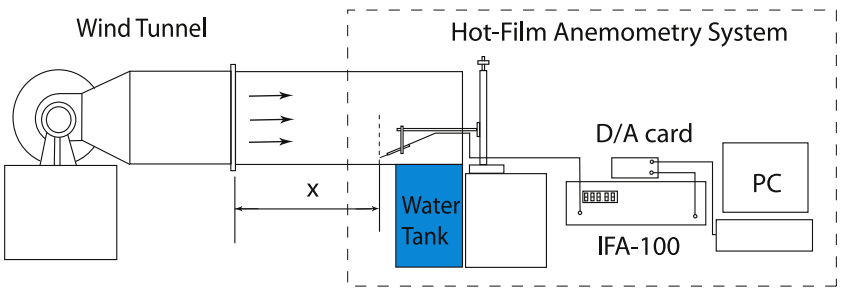

Fig. 4. Hot-film anemometry facility.

Author's personal copy

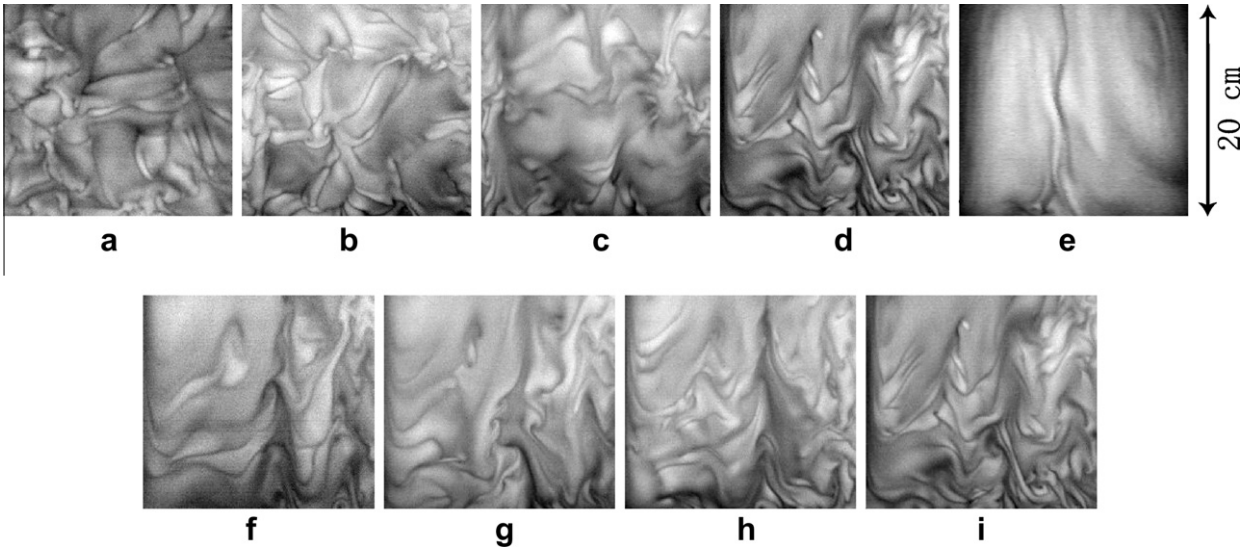

Fig. 5. Sample temperature fields obtained at different wind speeds and heat fluxes: (a) 0 m/s, 719 W/m^2, (b) 1 m/s, 754 W/m^2, (c) 2 m/s, 1030 W/m^2, (d) 3 m/s, 1290 W/m^2, (e) 4 m/s, 1860 W/m^2. Sample temperature fields obtained at a wind speed of 3 m/s. The heat fluxes are: (f) 681 W/m^2, (g) 1010 W/m^2, (h) 1150 W/m^2, and (i) 1290 W/m^2. The wind direction is from bottom to top.

Ra. Hence, the observed decrease in structure size is the expected decrease in length scale caused by an increase in the driving parameter, *Ra*.

3.2. Statistics versus heat flux

The rms and skewness of the temperature fields are computed using Eqs. (9) and (10), each of which requires subtraction of a mean temperature. There is, however, some finite variation in temperature in each of the three directions (i,j,k) of the image sequences. Here (i,j) are the down-stream and cross-stream directions, respectively, and k is time. The variation in the i and j directions is quantified in Fig. 6(a) where the maximum temperature difference ΔT in each of these directions is plotted versus U. Here ΔT is computed by first obtaining the maximum temperature difference in each row (column) and then obtaining the average of those maxima over all rows (columns) in an image sequence. The variation in time is revealed in Fig. 6(b) where the temperature of the center pixel $i, j = (104, 113)$ is plotted versus time. Of the three indices (i,j,k), Fig. 6(a) and (b) reveal that the variation in the downstream direction, i, is the largest, and hence averaging in this direction is unwise.

To compute σ and γ, the following procedure was followed. First, for each image sequence, the time trace for temperature for each pixel was detrended. As shown in Fig. 6(a), these plots are linear (for the relatively short durations of the sequences considered here), and hence a linear fit was obtained and the value of that fit subtracted from each point in time in that pixel's time trace. Because of the large variation in the downstream direction, statistics were computed only from a single row of pixels. Here, the middle row ($i = 104$) was used. The image sequence was detrended, the average of each row was subtracted from each pixel in that row, and the process repeated for each row # 104 in each image. Then these 96 rows were used to compute σ and γ for that image sequence.

Plots of σ versus q'' are presented in Fig. 7(a) revealing an increase in σ with q'' for all wind speeds. The 0, 1 and 2 m/s data collapse, and a single linear fit is presented for these wind speeds, while the 3 and 4 m/s data sets each have their own linear fit. Skewness is plotted versus heat flux in Fig. 7(b). Two data clouds can be observed in this plot, one for the $U = 0, 1, 2, 3$ m/s data sets, and the second for $U = 4$ m/s. An increasing trend is seen for skewness data for $U = 0$–3 m/s, although there is significant scatter.

The σ data presented in Fig. 7(a) is presented in dimensionless form in Fig. 8 as $\sigma/(T_b - T_s)$ versus *Ra*, where T_s is the surface temperature averaged over all 96 images of the image sequence. Only the 0–3 m/s data are plotted as discussed in Section 3.1. Here we scale σ to $(T_b - T_s)$ because this is a measure of the maximum possible variation in surface temperature, since the surface temperature can never exceed the bulk temperature in these experiments. This is a somewhat problematic approach since, strictly speaking, T_s is a dependent variable, and we would like to scale σ only to independent variables. A way around this would be to scale σ to $(T_b - T_a)$. However, because energy loss at the interface is due to both convection, and evaporation, σ is affected by the air humidity. Accordingly, we chose to scale to $(T_b - T_s)$ since this quantity bounds the rms in this problem. Fig. 8 shows that the scaled rms data increase linearly with *Ra* at each wind speed, and that the data separates with wind speed, $\sigma/(T_b - T_s)$ decreasing with U, at fixed *Ra*.

One of the motivations of this work was to attain a parameterization of σ in terms of the relevant dimensionless groups for mixed convection, namely (Ra, Re^*, Pr). Here we sought a power law scaling of the form:

$$\frac{\sigma}{T_b - T_s} = A Ra^m Re^{*n} Pr^o, \tag{17}$$

where *Ra*, Re^*, and *Pr* are based on water-side fluid properties. As noted in Section 2, we are using the Reynolds number based on friction velocity Re^*:

$$Re^* = \frac{u^* L}{\nu}, \tag{18}$$

to conform with the air/water interfacial literature, where the friction velocity is usually used.

To simplify the fitting process, the Prandtl number exponent was set to $o = -1/3$. This has been the generally accepted form of the Prandtl number dependence in turbulent thermal convection [41]. Deviations from this perfect $o = -1/3$ behavior have been reported [42], however the focus of the present work is to understand the *Ra* and Re^* scaling, and so we kept $o = -1/3$ in the fitting

Author's personal copy

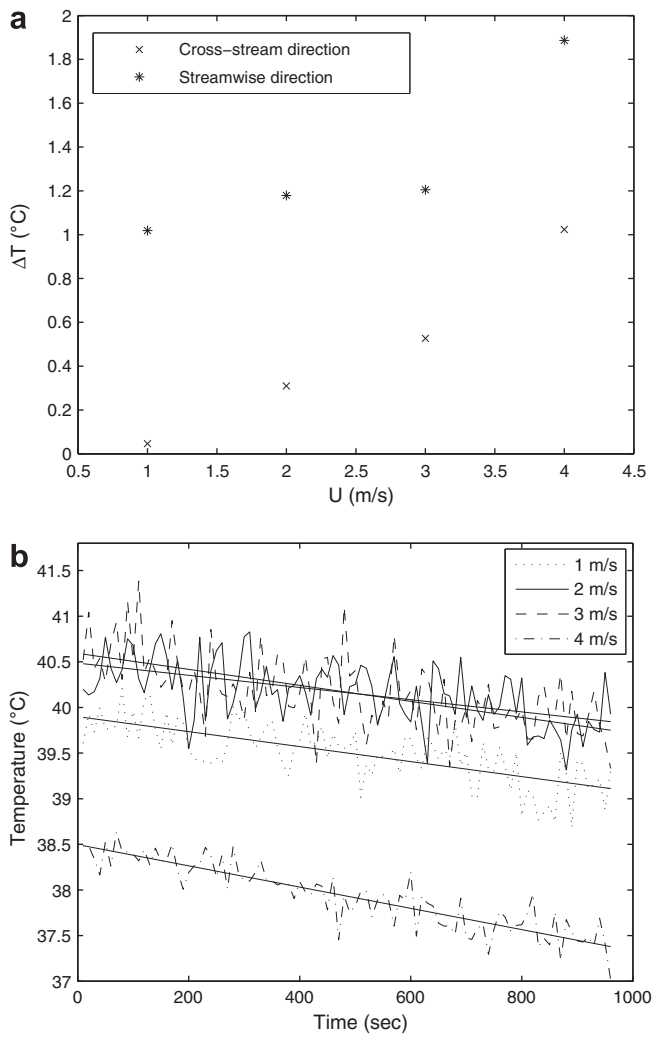

Fig. 6. The temperature difference in three dimensions, (a) the maximum temperature difference along the streamwise direction and the cross-stream direction and (b) the temporal temperature variation for: 1 m/s, 754 W/m^2, 2 m/s, 1028 W/m^2, 3 m/s, 1286 W/m^2 and 4 m/s, 1634 W/m^2.

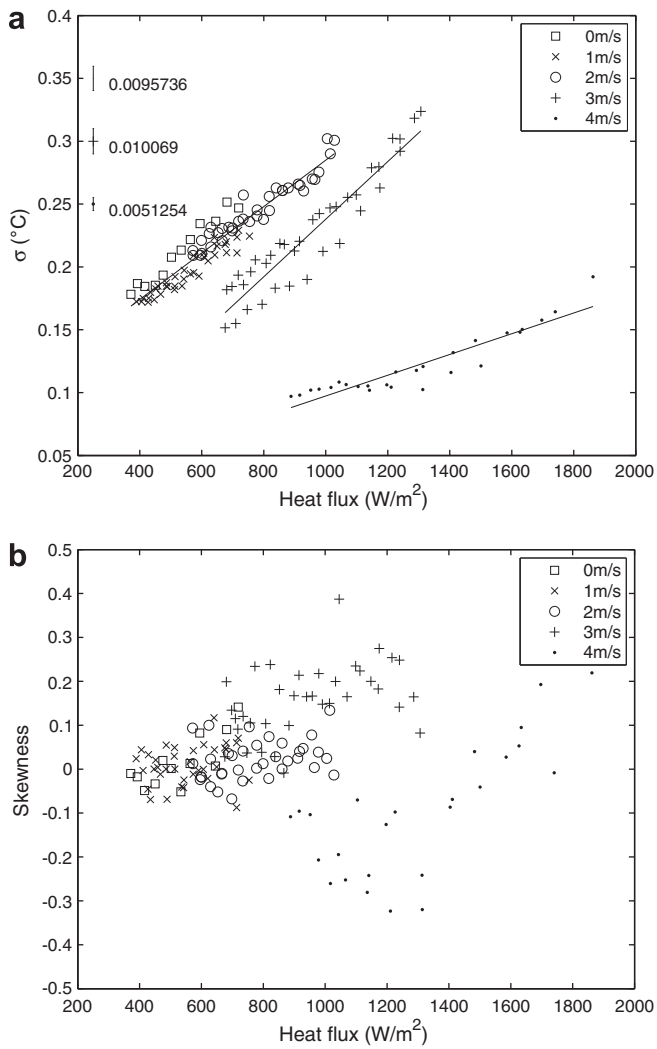

Fig. 7. The water temperature statistics versus heat flux, (a) root mean square of row #104 of the temperature field plotted against heat flux, the rms deviation of the data from the linear fit is presented as a vertical bar for each fit on the left side of the plot, (b) skewness of row #104 of the temperature field versus heat flux.

process. The temperature dependence of Pr is accounted for in the fitting process. Eq. (17) can be rearranged as:

$$\log\left[\frac{\sigma}{(T_b - T_s)Ra^m Pr^{-1/3}}\right] = \log A + n\log Re^*, \tag{19}$$

enabling use of a linear least squares fit to collapse the data. For a given value of m, a linear least squares fit provides (A, n). By iterating over m in increments of 0.01, the value of m was found which minimized the rms deviation of the data from the resulting fit. This value was $m = 0.37$, and the values of (A, n) at this optimal m were $A = 1.11 \times 10^{-3}$ and $n = -0.81$, giving:

$$\frac{\sigma}{T_b - T_s} = (1.11 \times 10^{-3})\, Ra^{0.37}\, Re^{*-0.81}\, Pr^{-1/3}, \tag{20}$$

which is plotted in Fig. 9(a). For simplicity, the exponents m and n can be rounded to 1/3 and −4/5. Doing this and obtaining a new prefactor, $A = 2.56 \times 10^{-3}$ gives:

$$\frac{\sigma}{T_b - T_s} = (2.56 \times 10^{-3}) Ra^{1/3} Re^{*-4/5}\, Pr^{-1/3}, \tag{21}$$

which is plotted with the data in Fig. 9(b) and shows good collapse of the data.

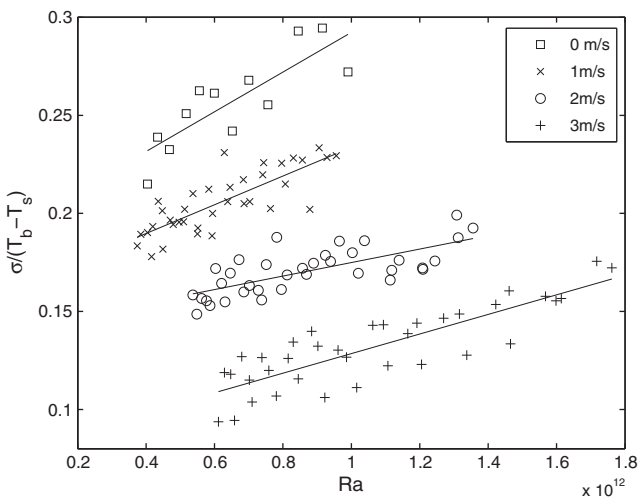

Fig. 8. Scaled rms surface temperature versus Rayleigh number.

Author's personal copy

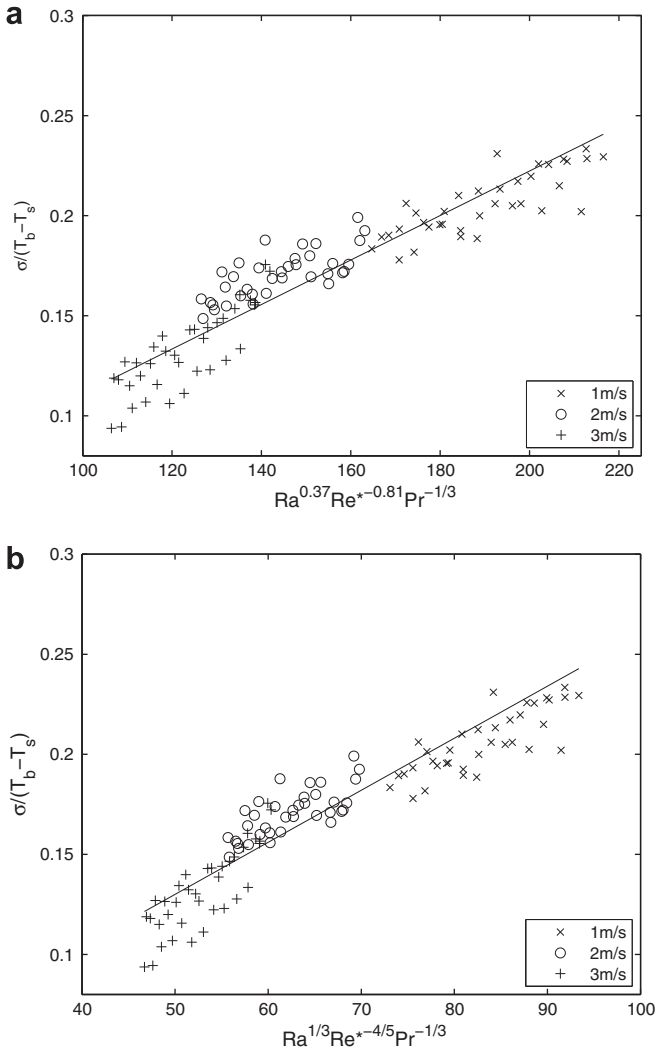

Fig. 9. Parameterization of scaled rms surface temperature: (a) scaled rms surface temperature versus $\left(Ra^{0.37}\,Re^{*-0.81}\,Pr^{-\frac{1}{3}}\right)$, (b) scaled rms surface temperature versus $\left(Ra^{\frac{1}{3}}\,Re^{*-\frac{4}{5}}\,Pr^{-\frac{1}{3}}\right)$.

It is noted that the parameterizations presented in Eqs. (20) and (21) diverge as wind speed goes to zero, while $\sigma/(T_b - T_s)$ remains bounded as $U \to 0$. The $U = 0$ data was not used when obtaining Eqs. (20) and (21). This choice was made to insure that the results were most applicable to mixed convection, the focus of this work; $U = 0$ is a pure natural convection case.

4. Discussion

The parameterizations of $\sigma/(T_b - T_s)$ to (Ra, Re^*, Pr) presented in Eqs. (20) and (21) and plotted in Fig. 9(a) and (b) are the main result of this work. The rms of the surface temperature field has never been parameterized in terms of both Ra and Re^*, for an air/water interface during mixed convection, and hence it is not possible to make a comparison with prior work. However, comparison to situations of pure natural convection can be made, although this comparison is necessarily incomplete.

Leighton et al. [10] obtained detailed statistics of temperature via a DNS study of free surface natural convection (i.e. $U = 0$). In their work, profiles of $\sigma/(T_b - T_s)$ were obtained for Ra ranging from 4.45×10^6 to 4.45×10^9. Over this range of Ra, $\sigma/(T_b - T_s)$ at the air/water interface was found to be relatively constant, ranging from 0.4 to 0.5, a 25% variation. In the present work, for the $U = 0$ case, we find $\sigma/(T_b - T_s)$ ranges from slightly more than *0.2* to slightly less than *0.3* as Ra varies from 4×10^{11} to 1×10^{12}. The disagreement in the magnitude of $\sigma/(T_b - T_s)$ is not large considering the difference in the magnitudes of Ra. However, if we apply the $\sigma/(T_b - T_s) \sim Ra^{1/3}$ variation obtained in the present work on the range of Ra explored by Leighton et al. [10] we would expect a factor of 10 variation in $\sigma/(T_b - T_s)$, which these authors do not observe. A possible source of this discrepancy concerns the heat flux which crosses the air/water interface. In the present work, this heat flux must exhibit some spatial variability since the surface has a spatial variation in temperature and, even if the heat transfer coefficient is constant, there will be a spatial variation in heat flux. In the work of Leighton et al. [10], a constant heat flux is imposed and this may serve to reduce changes in the scaled rms with Rayleigh number.

The $\sigma/(T_b - T_s)$ to (Ra, Re^*, Pr) parameterization obtained here may also be compared to the scaled rms of temperature obtained in turbulent Rayleigh–Bénard convection studies. In these studies, the rms is typically parameterized as:

$$\frac{\sigma}{\Delta T} = BRa_T^p, \tag{22}$$

where ΔT is the temperature difference between the hot and cold plates in the Rayleigh–Bénard apparatus, Ra_T is defined as:

$$Ra_T = \frac{g\beta\Delta TL^3}{\alpha\nu}, \tag{23}$$

and $\sigma/\Delta T$ is typically measured in the center of the Rayleigh–Bénard cell.

A range of values have been observed for the exponent p in Rayleigh–Bénard convection. For example, Niemela et al. [43] found $p = -0.145$, and Wu and Libchaber [44] found $p = -0.14$ for small aspect ratio cells and $p = -0.20$ for large aspect ratio cells. Du and Tong [45] found $p = -0.14$ for Rayleigh–Bénard convection in an apparatus with rough walls. A review of other results is presented in Daya and Ecke [46], who show that, for the studies reviewed, p is always negative. In contrast, in the present work the exponent for the Rayleigh number is positive (note that the exponent p in Eq. (22) is analogous to the exponent m in Eq. (17)). This is true both when $\sigma/(T_b - T_s)$ is parameterized in terms of Ra, as defined in Eq. (12), giving $m = 1/3$ and also when $\sigma/(T_b - T_s)$ is parameterized in terms of Ra_T, as defined in Eq. (23), which gives $m = 0.7$ for the present data. This is shown graphically in Fig. 10 where $\sigma/(T_b - T_s)$ is plotted against Ra_T, revealing an

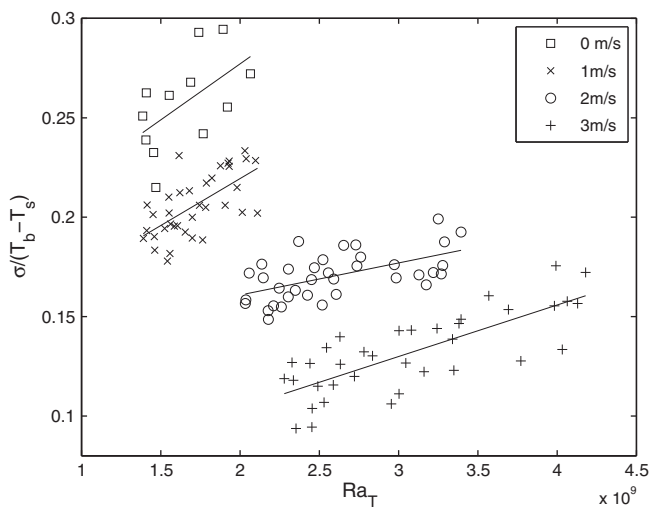

Fig. 10. Scaled rms surface temperature versus Ra_T.

Author's personal copy

increase in $\sigma/(T_b - T_s)$ with Ra_T for all wind speeds. Note that in Fig. 10 the value of ΔT used in the definition of Ra_T is $(T_b - T_s)$.

Rayleigh–Bénard convection differs from the present work in several ways. First, there is no forced convection. However, this is not the explanation for the difference in the sign of p, since this difference exists in the present work, even when $U = 0$ (*viz.* for pure natural convection). The thermal and hydrodynamic boundary conditions are also different between Rayleigh–Bénard convection and the present study. Thermally, in the Rayleigh–Bénard case, a constant temperature or constant heat flux boundary condition exists, while the present case considers an air/water interface which lacks a constant temperature or constant heat flux boundary condition. However, in the present case, the thermal boundary condition must lie somewhere between these two limiting cases, and many Rayleigh–Bénard convection studies have both a constant temperature and a constant heat flux boundary condition (top plate and bottom plate, respectively) in the same apparatus, and so this difference is unlikely to explain the difference in sign for p. The hydrodynamic boundary condition in a Rayleigh–Bénard apparatus is of the no-slip type, while the air/water interface is one of a finite elasticity when a surfactant is present. In a Rayleigh–Bénard apparatus, σ is measured in the bulk and approaches zero at the plate with a constant temperature boundary condition. In the present study, we measure σ at the apparatus "boundary" (the air–water interface), and it is this that is likely to be the cause of the difference in the sign of p since at the air/water interface, the turbulence necessarily becomes two-dimensional in nature, while σ in Rayleigh–Bénard convection is measured in the bulk where the turbulence is three dimensional.

One of the objectives of this paper was to determine how well the rms of the surface temperature field could be used as a remotely sensed signature, used to obtain surface heat flux. No general collapse of the data is seen in Fig. 7(a) and (b), showing that the surface temperature statistics are not solely dependent on the heat flux across the air/water interface. However, the data for 0, 1 and 2 m/s do collapse with heat flux. This linear relationship between σ and q'' may possibly be applied to the remote sensing field for this limited range of wind speeds. However, it is noted that waves, currents, solar irradiation and other factors would make it difficult to apply these results to the field, and further research on these environmental influences is needed before this application is realized.

The outliers for 4 m/s in the plots presented in Fig. 7(a) and (b) may be due to tank edge effects. The wind/water tunnel used here employed a small tank to reduce the surface shear on the air/water interface so as to maintain a surfactant-covered surface. The results seen at 4 m/s reveal what appears to be a type of recirculation in the plane of the interface that most likely would not be observed in a much longer tunnel. However, lengthening the tunnel was not pursued here due to the likelihood of the formation of a Reynolds ridge.

5. Conclusion

A surfactant-covered water surface temperature field was investigated under mixed convection conditions, a condition common to small inland lakes, reservoirs and cooling ponds. A parameterization between the scaled rms of the surface temperature field and (Ra, Re^*, Pr) was developed, the first of its kind. The unscaled rms was found to increase linearly with heat flux for wind speeds $U = 0$–4 m/s, and the behavior of the unscaled rms was essentially identical for wind speeds $U = 0$–2 m/s.

Acknowledgment

This work was supported by the Department of Energy through the Savannah River National Laboratory.

References

[1] A. Wuest, A. Lorke, Small-scale hydrodynamics in lakes, Annu. Rev. Fluid Mech. 35 (2003) 373–412.
[2] B.R. Thomas, E.C. Kent, V.R. Swail, D.I. Berry, Trends in ship wind speeds adjusted for observation method and height, Int. J. Climatol. 28 (2008) 747–767.
[3] K. Klink, Climatological mean and interannual variance of United States surface wind speed, direction and velocity, Int. J. Climatol. 19 (1999) 471–488.
[4] J.D. Lenters, T.K. Kratz, C.J. Bowser, Effects of climate variability on lake evaporation: results from a long-term energy budget study of Sparkling Lake, northern Wisconsin (USA), J. Hydrol. 308 (2005) 168–195.
[5] D.M. Deaves, I.G. Lines, The nature and frequency of low wind speed conditions, J. Wind Eng. 73 (1998) 1–29.
[6] U. Schimpf, C. Garbe, B. Jähne, Investigation of transport processes across the sea surface microlayer by infrared imagery, J. Geophys. Res. 109 (C08S13) (2004) 1–14.
[7] C.S. Garbe, U. Schimpf, B. Jähne, A surface renewal model to analyze infrared image sequences of the ocean surface for the study of air–sea heat and gas exchange, J. Geophys. Res. 109 (C08S15) (2004) 1–18.
[8] J.R. Saylor, G.B. Smith, K.A. Flack, The effect of a surfactant monolayer on the temperature field of a water surface undergoing evaporation, Int. J. Heat Mass Trans. 43 (2000) 3073–3086.
[9] J.R. Saylor, G.B. Smith, K.A. Flack, An experimental investigation of the surface temperature field during evaporative convection, Phys. Fluids 13 (2001) 428–439.
[10] R.I. Leighton, G.B. Smith, R.A. Handler, Direct numerical simulation of free convection beneath an air–water interface at low Rayleigh numbers, Phys. Fluids 15 (10) (2003) 3181–3193.
[11] R.A. Handler, G.B. Smith, R.I. Leighton, The thermal structure of an air–water interface at low wind speeds, Tellus 53A (2001) 233–244.
[12] T.A. Conover, J.R. Saylor, Infrared imaging of a solid phase surfactant monolayer, Langmuir 22 (2006) 6881–6886.
[13] R.A. Handler, J.R. Saylor, R.I. Leighton, A.L. Rovelstad, Transport of a passive scalar at a shear-free boundary in fully developed turbulent open channel flow, Phys. Fluids 11 (1999) 2607–2625.
[14] R.A. Handler, R.I. Leighton, G.B. Smith, R. Nagaosa, Surfactant effects on passive scalar transport in a fully developed turbulent flow, Int. J. Heat Mass Transfer 46 (2003) 2219–2238.
[15] L.I. Enstad, R. Nagaosa, G. Alendal, Turbulence structure and mass transfer across a sheared air–water interface in wind-driven turbulence, Phys. Fluids 18 (2006) 055106.
[16] H.D. Downing, D. Williams, Optical constants of water in the infrared, J. Geophys. Res. 80 (1975) 1656–1661.
[17] E.K. Rideal, On the influence of thin surface films on the evaporation of water, J. Phys. Chem. 29 (1925) 1585–1588.
[18] V.K. La Mer (Ed.), Retardation of Evaporation by Monolayers: Transport Processes, Academic Press, New York, 1962.
[19] T.G. Springer, R.L. Pigford, Influence of surface turbulence and surfactants on gas transport through liquid interfaces, Ind. Eng. Chem. Fund. 9 (1970) 458–465.
[20] U. Navon, J.B. Fenn, Interfacial mass and heat transfer during evaporation: II. effect of monomolecular films on natural convection in water, AIChE J. 17 (1971) 137–140.
[21] G.T. Barnes, The effects of monolayers on the evaporation of liquids, Adv. Colloid Interface Sci. 25 (1986) 89–200.
[22] G.T. Barnes, Permeation through monolayers, Colloids Surfaces A: Physiochem. Eng. Aspects 126 (1997) 149–158.
[23] K.B. Katsaros, W.D. Garrett, Effects of organic surface films on evaporation and thermal structure of water in free and forced convection, Int. J. Heat Mass Transfer 25 (1982) 1661–1670.
[24] W.R. Barger, A review of experimental observations and remaining questions concerning formation, persistence, and disappearance of sea slicks, NRL Report 9313, Naval Research Laboratory, Washington DC, 1991, pp.1–46.
[25] J.R. Saylor, Determining liquid substrate cleanliness using infrared imaging, Rev. Sci. Instrum. 72 (2001) 4408–4414.
[26] O. Reynolds, Papers on Mechanical and Physical Subjects, vol. 1, University Press, Cambridge, 1900. pp. 411–412.
[27] P.K. Kundu, Fluid Mechanics, Academic Press, San Diego, 1990.
[28] G.L. Gaines Jr., Insoluble Monolayers at Liquid–Gas Interfaces, John Wiley and Sons, New York, NY, 1966.
[29] A.W. Adamson, Physical Chemistry of Surfaces, John Wiley and Sons, New York, NY, 1990.
[30] J.H. Brooks, A.E. Alexander, The spreading behavior and crystalline phases of fatty alcohols, in: Retardation of Evaporation by Monolayers: Transport Processes, Academic Press, 1962, pp. 245–269.
[31] B.R. Munson, D.F. Young, T.H. Okiishi, Fundamentals of Fluid Mechanics, fourth ed., Wiley, New York, 2002.
[32] F. Heslot, B. Castaing, A. Libchaber, Transitions to turbulence in helium gas, Phys. Rev. A 36 (1987) 5870–5873.
[33] J. Niemela, High Rayleigh number thermal convection, J. Low Temp. Phys. 134 (1–2) (2004) 447–456.
[34] B. Jähne, K.O. Münnich, U. Siegenthaler, Measurements of gas exchange and momentum transfer in a circular wind-water tunnel, Tellus 31 (1979) 321–329.

Author's personal copy

[35] A. Bejan, Convection Heat Transfer, second ed., John Wiley and Sons Inc., New York, 1995.
[36] E.L. Deacon, Gas transfer to and across an air–water interface, Tellus 29 (1977) 363–374.
[37] H. Grassl, The dependence of the measured cool skin of the ocean on wind stress and heat flux, Boundary-Lay. Metrol. 10 (1976) 465–475.
[38] G. Comte-Bellot, Hot-wire anemometry, Annu. Rev. Fluid Mech. 8 (1976) 209–231.
[39] H.H. Bruun, Hot-Wire Anemometry, Oxford University Press, New York, 1995.
[40] C.F. Lange, F. Durst, M. Breuer, Correction of hot-wire measurements in the near-wall region, Exp. Fluids 26 (1999) 475–477.
[41] R.H. Kraichnan, Turbulent thermal convection at arbitrary Prandtl number, Phys. Fluids 5 (1962) 1374–1389.
[42] Z.A. Daya, R.E. Ecke, Prandtl-number dependence of interior temperature and velocity fluctuations in turbulent convection, Phys. Rev. E 66 (2002) 045301.1–045301.4.
[43] J.J. Niemela, L. Skrbek, K.R. Sreenivasan, R.J. Donnelly, Turbulent convection at very high Rayleigh numbers, Nature 404 (2000) 837–840.
[44] X.Z. Wu, A. Libchaber, Scaling relations in thermal turbulence: the aspect-ratio dependence, Phys. Rev. A 45 (1992) 842–845.
[45] Y.B. Du, P. Tong, Temperature fluctuations in a convection cell with rough upper and lower surfaces, Phys. Rev. E 63 (2001) 046303.
[46] Z.A. Daya, R.E. Ecke, Does turbulent convection feel the shape of the container? Phys. Rev. Lett. 87 (2001) 184501.